

Roles of magnetic coupling and spin-orbit torque in the electrical manipulation of exchange bias in a Pt/Co/IrMn heterostructure

Eunchong Baek,¹ Suhyeok An¹, Soobeom Lee,² Dongryul Kim,¹ Jun-Su Kim,¹ Ki-Seung Lee,³ and Chun-Yeol You^{1,*}

¹*Department of Physics and Chemistry, DGIST, Daegu 42988, Republic of Korea*

²*Basic Sciences Research Center, DGIST, Daegu 42988, Republic of Korea*

³*Emerging Materials Science Research Center, DGIST, Daegu 42988, Republic of Korea*



(Received 22 March 2023; accepted 19 May 2023; published 1 June 2023)

Heavy-metal/ferromagnet/antiferromagnet heterostructures have attracted significant attention in manipulating antiferromagnetic ordering electrically. We report electric control of the exchange bias field along both the out-of-plane and in-plane directions in Pt/Co/IrMn with assist magnetic fields. Experiments with different directions and amplitudes of the assist magnetic field show the role of magnetic coupling between ferromagnet and antiferromagnet spins. Furthermore, we find that the magnitude and direction of the exchange bias can be manipulated by the magnitude of the current pulse. The observed results can be explained based on a numerical macrospin model; the antiferromagnetic spins are excited and precessed from their ground state via the spin-orbit torque-driven oscillation and are reoriented, being mediated by magnetic coupling with the ferromagnet. Our results provide an approach to achieve electrical omnidirectional exchange bias manipulation and an understanding of the spin dynamics at the antiferromagnet-ferromagnet interface.

DOI: [10.1103/PhysRevB.107.214403](https://doi.org/10.1103/PhysRevB.107.214403)

Various intriguing physical phenomena of antiferromagnetic (AFM) materials, such as ultrafast spin dynamics up to the terahertz (THz) range, negligible stray fields, and robustness to an external magnetic field, provide a new paradigm in the field of spintronics [1–3]. To achieve AFM spintronics devices, electrical control of the magnetic configuration of the AFM material is an integral part. In recent years, spin-orbit torque (SOT), which is induced by spin current via spin-orbit coupling, has been one of the pivotal approaches to electrical manipulation of AFM spins [4–13]. Based on this, a heavy-metal (HM)/ferromagnet (FM)/AFM heterostructure is an excellent platform to study the electrical manipulation of AFM spins because the HM is a source of SOT by electric current injection, which is the origin of AFM spin excitation [14–20]. Moreover, the interfacial spin configuration can be experimentally probed by the magnitude and direction of the exchange bias (EB) field between the FM/AFM interface using hysteresis loop measurements under applied out-of-plane and in-plane magnetic fields. Previous works have demonstrated the reversal of the EB field by SOT in perpendicularly magnetized HM/FM/AFM heterostructures [16–18]. However, no consensus has been reached on the underlying mechanism behind them, owing to the complex interplay between SOT, magnetic coupling, and thermal fluctuation of the interface spins. This study aims to clarify and separate experimentally the roles of magnetic coupling and SOT in the HM/FM/AFM heterostructure. We demonstrated electrical manipulation of the exchange bias field along both out-of-plane and in-plane directions by utilizing a magnetic field that exceeds the uniaxial ferromagnetic anisotropy. The

direction and magnitude of the EB field after the manipulation procedure were obtained by separately measuring the hysteresis loops under applied in-plane and out-of-plane magnetic fields. Furthermore, we determined that the sign change of the EB field occurred when the electric current exceeded a certain critical value. Based on the experimentally observed results and our macrospin model calculation, we elucidated the role of magnetic coupling between the FM/AFM and described how SOT contributed to the electrical manipulation of the exchange bias in the HM/FM/AFM heterostructure.

A thin film stack of Ta (3 nm)/Pt (5 nm)/Co (1.2 nm)/IrMn (8 nm)/Ta (2 nm) is deposited on a SiO₂ substrate by dc magnetron sputtering as an HM/FM/AFM heterostructure. The platinum layer serves as a main spin current source, owing to its relatively larger spin-orbit coupling and smaller resistivity than those of IrMn [21]. Perpendicular magnetic anisotropy occurs in the 1.2-nm-thick cobalt FM layer, which requires a magnetic field of 1 T for aligning the cobalt magnetization toward its hard-axis (in-plane) (see Supplemental Material Fig. S1 [22]). The IrMn AFM layer is exchange-coupled to the cobalt layer. After the deposition of the thin-film stack, the Hall cross-bar devices are patterned via standard photolithography and argon ion etching [Fig. 1(a)]. Charge current flows in the channel with a 5- μ m width, while the Hall voltage is detected in the transverse line with a 2- μ m width. In this scheme, the longitudinal charge current (x direction) induces transverse spin polarization (y direction) via spin-orbit coupling, and the spin current propagates along the z direction [see the coordinate system in Fig. 1(a)]. The generated spin current clearly exerts the antidamping torque onto the HM/FM interface. In addition, we believe the spin current also arrives at the FM/AFM interface through a thin cobalt layer because

*cyyou@dgist.ac.kr

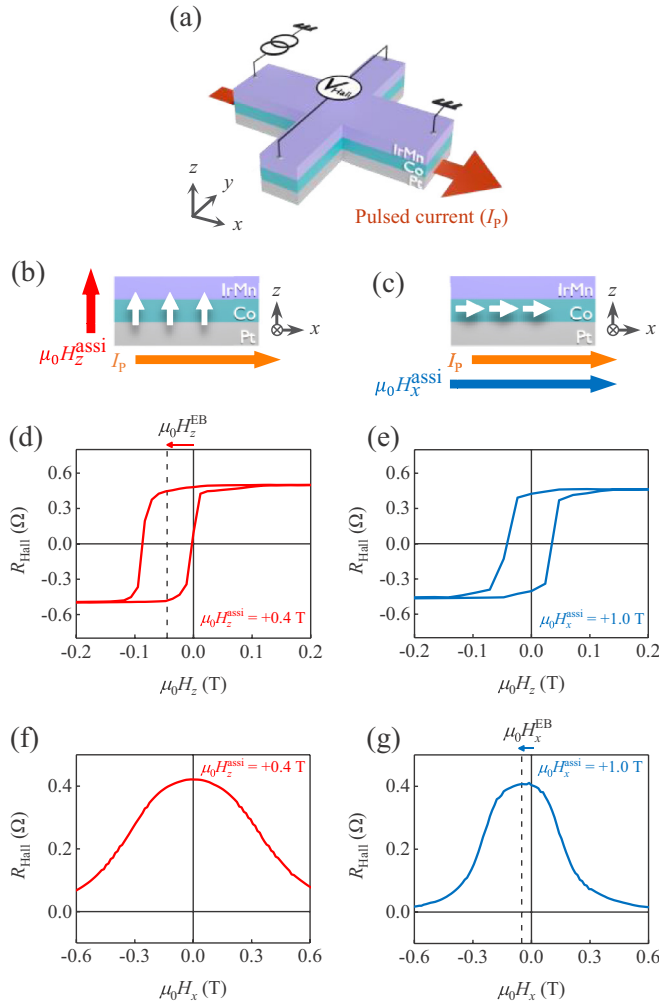


FIG. 1. (a) Hall bar structure and measurement scheme where I_p is the pulsed current with the coordinate system. (b) and (c) Schematics of the writing procedure in the Pt/Co/IrMn heterostructure. Here, (b) the $\mu_0 H_z^{\text{ass}}$ is the out-of-plane writing assist magnetic field and (c) the $\mu_0 H_x^{\text{ass}}$ is the in-plane writing assist magnetic field. Both writing assist fields are only applied during the writing procedure. (d) and (e) Hall resistance (R_{Hall}) versus magnetic field along the z -axis ($\mu_0 H_z$) after the writing procedure with an I_p of +23 mA under a (d) $\mu_0 H_z^{\text{ass}}$ of +0.4 T and an (e) $\mu_0 H_x^{\text{ass}}$ of +1.0 T. $\mu_0 H_z^{\text{EB}}$ is the exchange bias field established in the + z direction. (f) and (g) R_{Hall} versus magnetic field along the x -axis ($\mu_0 H_x$) after the writing procedure with an I_p of +23 mA under (f) a $\mu_0 H_z^{\text{ass}}$ of +0.4 T and (g) a $\mu_0 H_x^{\text{ass}}$ of +1.0 T. $\mu_0 H_x^{\text{EB}}$ is the EB field established in the + x direction.

the thickness of the cobalt layer is less than the spin diffusion length in the cobalt layer [16], and our experimental results cannot be explained without the presence of finite spin torque in the AFM layer.

Here, we describe the detailed procedures of our experiments. Whole experiments are performed in the order of (i) writing and (ii) reading processes. For the writing process, we proceed with the electrical manipulation of the EB [Figs. 1(b) and 1(c)]. Similar to the experimental procedure of conventional SOT-induced magnetization reversal [24,25], a current pulse (I_p) is applied along the x -axis under a writing assist magnetic field (H^{ass}). H^{ass} is turned off after I_p application,

and the current pulse duration is set to a value of 1 ms in this study. Unlike the conventional SOT-induced magnetization reversal method, we examine the manipulation of the EB with two different directions of the H^{ass} : out-of-plane (z -axis, $\mu_0 H_z^{\text{ass}}$) and in-plane (x -axis, $\mu_0 H_x^{\text{ass}}$). In the two cases, an I_p of +23 mA (current density, 6×10^{11} A/m²) is applied under a $\mu_0 H_z^{\text{ass}}$ of +0.4 T [Fig. 1(b)] and $\mu_0 H_x^{\text{ass}}$ of +1.0 T [Fig. 1(c)], respectively. After the writing procedure, we measure the spin configurations of the AFM, which itself occurs via the magnitude and direction of the EB field.

To measure the EB field, we now conduct reading of the EB field by measuring the anomalous Hall resistance (R_{Hall}) as a function of both the out-of-plane (H_z) and in-plane (H_x) external magnetic fields. We obtained four different $R_{\text{Hall}}-H$ loops in Figs. 1(d)–1(g) as follows: Figure 1(d) and 1(e), and Figs. 1(f) and 1(g) show the $R_{\text{Hall}}-H_z$ ($-H_x$) curves after the writing process with $\mu_0 H_z^{\text{ass}}$ and $\mu_0 H_x^{\text{ass}}$, respectively. Figure 1(d) shows the result of a current pulse application under a $\mu_0 H_z^{\text{ass}}$ of 0.4 T, which exhibits a clear square hysteresis in R_{Hall} . A shift in the hysteresis loop (z -axis EB field, $\mu_0 H_z^{\text{EB}}$) is observed, indicating that a negative $\mu_0 H_z^{\text{EB}}$ is established at the FM/AFM interface at room temperature. In contrast with the former case, after the writing procedure with a current pulse under the $\mu_0 H_x^{\text{ass}}$ [Fig. 1(c)], the EB in the measured anomalous Hall curve is quenched, i.e., $\mu_0 H_z^{\text{EB}} = 0$ [Fig. 1(e)].

Subsequently, we focus on the $R_{\text{Hall}}-H_x$ loop measurement. We note that R_{Hall} typically reflects out-of-plane magnetization components, and the in-plane magnetic field inclines the magnetizations from the easy axis (z -axis), producing a decrease in the magnitude of R_{Hall} . As shown in Fig. 1(f), the $R_{\text{Hall}}-H_x$ loop is symmetric with respect to the sign of the x -axis, representing the result of the writing procedure under the $\mu_0 H_z^{\text{ass}}$ [Fig. 1(b)] case. However, Fig. 1(g) shows a shifted $R_{\text{Hall}}-H_x$ loop (x -axis EB field, $\mu_0 H_x^{\text{EB}}$) for the case where the EB is manipulated under a $\mu_0 H_x^{\text{ass}}$ of +1.0 T [Fig. 1(c)]. Because the magnitude of R_{Hall} reflects the out-of-plane component of the magnetization of cobalt, the left-shifted loop is interpreted as the interfacial FM spins being tilted by negative $\mu_0 H_x^{\text{EB}}$ after the writing procedure with a $\mu_0 H_x^{\text{ass}}$ of +1.0 T. Furthermore, we also obtained the positive EB fields for the x - and z -axes with negative $\mu_0 H_x^{\text{ass}}$ and $\mu_0 H_z^{\text{ass}}$, respectively (not shown here). From the experimental results, we can hypothesize that the manipulation of the EB in both out of plane and in plane in a perpendicularly magnetized Pt/Co/IrMn system is successfully achieved.

Hereafter, we disentangle the roles of the H^{ass} and electric current in the electrical manipulation of the EB in the HM/FM/AFM heterostructure. Initially, we investigate electrical switching of the EB field by varying the amplitude of the H^{ass} while maintaining a constant I_p amplitude of +23 mA. In this discussion, the EB manipulations along the z -axis and x -axis are separately demonstrated. For the z -axis EB manipulation, the initial state of the EB field is set to positive in the z direction ($\mu_0 H_z^{\text{EB}} = +41.5$ mT) by applying I_p with a $\mu_0 H_z^{\text{ass}}$ of -0.4 T [Fig. 2(a), black line]. After initialization, writing procedures are performed with various amplitudes of positive $\mu_0 H_z^{\text{ass}}$ ranging from +0.1 T to +0.4 T. Figure 2(a) shows the typical anomalous Hall loops for the initial state (black

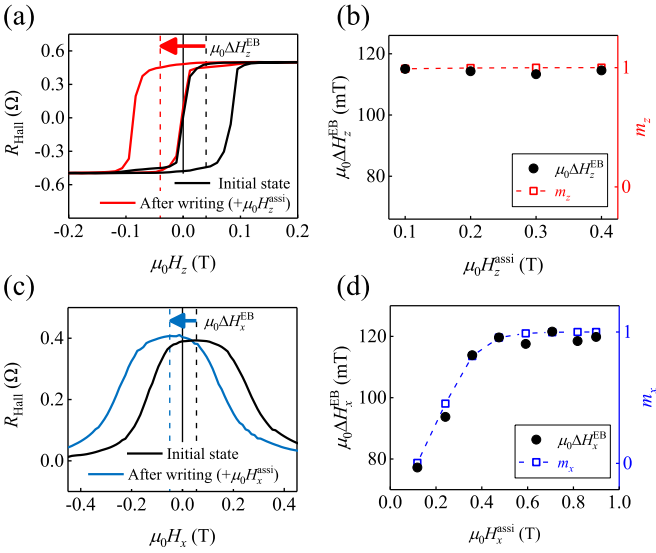


FIG. 2. (a) Curves showing R_{Hall} versus $\mu_0 H_z$ at an initial state set by applying an I_p under a $\mu_0 H_z^{\text{ass}_i}$ of -0.4 T (black line) and after writing under a $\mu_0 H_z^{\text{ass}_i}$ of $+0.4$ T from the initial state (red line). Here, $\mu_0 \Delta H_z^{\text{EB}} = \mu_0 H_z^{\text{EB}}(\mu_0 H_z^{\text{ass}_i} = -0.4 \text{ T}) - \mu_0 H_z^{\text{EB}}(\mu_0 H_z^{\text{ass}_i})$. (b) $\mu_0 H_z^{\text{ass}_i}$ -dependent $\mu_0 \Delta H_z^{\text{EB}}$ (black circles) and m_z (red open squares with dashed line). (c) Curves showing R_{Hall} versus $\mu_0 H_x$ at an initial state set by applying an I_p under a $\mu_0 H_x^{\text{ass}_i}$ of -1.0 T (black line) and after writing under a $\mu_0 H_x^{\text{ass}_i}$ of $+1.0$ T from the initial state (blue line). Here, $\mu_0 \Delta H_x^{\text{EB}} = \mu_0 H_x^{\text{EB}}(\mu_0 H_x^{\text{ass}_i} = -1.0 \text{ T}) - \mu_0 H_x^{\text{EB}}(\mu_0 H_x^{\text{ass}_i})$. (d) $\mu_0 H_x^{\text{ass}_i}$ -dependent $\mu_0 \Delta H_x^{\text{EB}}$ (black circles) and m_x (blue open squares with dashed line). I_p amplitudes are always set to $+23$ mA.

line) and after writing (red line) with a positive $\mu_0 H_z^{\text{ass}_i}$, where the EB field is switched from positive to negative. To quantify the dependence of the $\mu_0 H_z^{\text{EB}}$ on $\mu_0 H_z^{\text{ass}_i}$, $\mu_0 \Delta H_z^{\text{EB}} [= \mu_0 H_z^{\text{EB}}(\mu_0 H_z^{\text{ass}_i} = -0.4 \text{ T}) - \mu_0 H_z^{\text{EB}}(\mu_0 H_z^{\text{ass}_i})]$ is plotted as a function of $\mu_0 H_z^{\text{ass}_i}$ [Fig. 2(b)]. $\mu_0 \Delta H_z^{\text{EB}}$ is almost constant across the entire $\mu_0 H_z^{\text{ass}_i}$ range. Now we can focus on the magnetic configuration of the FM layer during the writing procedure to determine the role of the H^{ass_i} in the EB manipulation. We monitored R_{Hall} signals during the writing process ($I_p = 23$ mA with a $H_z^{\text{ass}_i}$ of $+0.1$ to $+0.4$ T), which corresponds to the z component of FM layer magnetization (m_z). The normalized R_{Hall} with $R_{\text{Hall, Max}}$ ($I_p = 23$ mA and $H_z^{\text{ass}_i} = 0.4$ T), which is m_z , are depicted in Fig. 2(b) as red open squares, and it is constantly one, which means the magnetization is fully saturated along the $+z$ direction during the writing processes despite the magnitude of the $H_z^{\text{ass}_i}$. We will discuss the physical meaning of these two results after we explain Figs. 2(c) and 2(d) for the x -axis EB manipulations.

Similar to z -axis EB manipulation, the initial state of the EB field is set to positive ($\mu_0 H_x^{\text{EB}} = +55.0$ mT) by I_p application with a $\mu_0 H_x^{\text{ass}_i}$ of -1.0 T. Subsequently, writing procedures are carried out with a positive $\mu_0 H_x^{\text{ass}_i}$ amplitude ranging from $+0.1$ T to $+0.9$ T. Figure 2(c) represents the measured $R_{\text{Hall}}-H_x$ loops for the initial state (black line) and after writing (blue line) with a positive $\mu_0 H_x^{\text{ass}_i}$ of $+1.0$ T. The blue line in Fig. 2(c) shows a loop that has shifted

to the left, indicating that $\mu_0 H_x^{\text{EB}}$ has changed to a negative value with a $\mu_0 H_x^{\text{ass}_i}$ of $+1.0$ T. We plotted $\mu_0 \Delta H_x^{\text{EB}}$, which is defined in the same way as $\mu_0 \Delta H_z^{\text{EB}}$, with black circles in Fig. 2(d), as a function of the magnitude of the $\mu_0 H_x^{\text{ass}_i}$. $\mu_0 \Delta H_x^{\text{EB}}$ is strongly dependent on the magnitude of the $\mu_0 H_x^{\text{ass}_i}$, increasing gradually with the $\mu_0 H_x^{\text{ass}_i}$ and saturating above $+0.4$ T. This is clearly a different behavior compared with the z -axis EB manipulation cases, as shown in Fig. 2(b). We measured R_{Hall} signals for a $\mu_0 H_x^{\text{ass}_i}$ of $+0.1$ to $+1.0$ T with an I_p of 23 mA during the writing process and show the x components of FM layer magnetization as $m_x = \{1 - [R_{\text{Hall}}(\mu_0 H_x^{\text{ass}_i})/R_{\text{Hall}}(0)]^2\}^{1/2}$ in Fig. 2(d) with blue open squares. Here, $\{1 - [R_{\text{Hall}}(\mu_0 H_x^{\text{ass}_i})/R_{\text{Hall}}(0)]^2\}^{1/2}$ reflects the contribution of m_x during the writing processes with a different $\mu_0 H_x^{\text{ass}_i}$. It begins to increase with an increasing $\mu_0 H_x^{\text{ass}_i}$ and is saturated above $+0.4$ T. As shown in Figs. 2(b) and 2(d), $\mu_0 \Delta H_{x,z}^{\text{EB}}$ exhibits noticeable correlations with m_x and m_z during the write procedures, respectively. This implies that the direction and magnitude of the EB field are mainly determined by the orientation of the magnetization of the FM layer during the writing procedure rather than the H^{ass_i} direction itself. In other words, the degree of alignment of the magnetization of the FM layer to the x or z directions determines the direction and strength of the EB fields. The correlations between $\mu_0 \Delta H_{x,z}^{\text{EB}}$ and $m_{x,z}$ are clear evidence of our claim.

Next, we perform electric current-dependent EB manipulation experiments to show the role of electric current in EB manipulation. The initial state of the EB field is set to positive in the z direction by applying an I_p of $+23$ mA with a $\mu_0 H_z^{\text{ass}_i}$ of -0.4 T. This initial state is the same as that of the z -axis EB manipulation shown by the black line in Fig. 2(a). Subsequently, we conduct writing procedures under various magnitudes of I_p . Figures 3(a)–3(c) shows the $R_{\text{Hall}}-H_z$ loops after writing with an I_p of $+14$ mA [Fig. 3(a), orange curves], $+16$ mA [Fig. 3(b), magenta curves], and $+23$ mA [Fig. 3(c), red curves], respectively, under a $\mu_0 H_z^{\text{ass}_i}$ of $+0.4$ T. Unlike the case of I_p of $+23$ mA, the hysteresis loops are partially shifted after applications of I_p of $+14$ mA and $+16$ mA. For more clarity, we quantified the degree of partial shift by presenting $\mu_0 H_z^{\text{EB}}$ as a function of the magnitude of I_p for a $\mu_0 H_z^{\text{EB}}$ of $+0.4$ T and -0.4 T [Fig. 3(d)]. The measurement protocol for black squares (purple triangles) in Fig. 3(d) is as follows: First, the initial state of the EB field is set to positive (negative) in the z direction. Next, as the writing proceeds, I_p is swept from $+2$ mA to $+23$ mA and from -2 mA to -23 mA under the applied $\mu_0 H_z^{\text{ass}_i}$ of $+(-)0.4$ T. After each writing, the $\mu_0 H_z^{\text{EB}}$ is evaluated from a shift in the R_{Hall} -versus- H_z curve. As shown in Fig. 3(d), regardless of the direction of the $\mu_0 H_z^{\text{ass}_i}$, $\mu_0 H_z^{\text{EB}}$ begins to change when I_p exceeds ± 10 mA, and reaches saturation at ± 20 mA, which is the signature of the formation of a multidomain state in the current-induced manipulation of AFM ordering [26,27]. Surprisingly, the switching direction of the EB field is independent of the current polarity. An electric current in the Pt/Co/IrMn system generates a transverse spin current via spin-orbit coupling, where the electric current polarity determines the polarity of the spin current. Nevertheless, switching of the EB field is not affected by the orientation of propagating spins. This behavior is similar to thermal-assisted effects, such

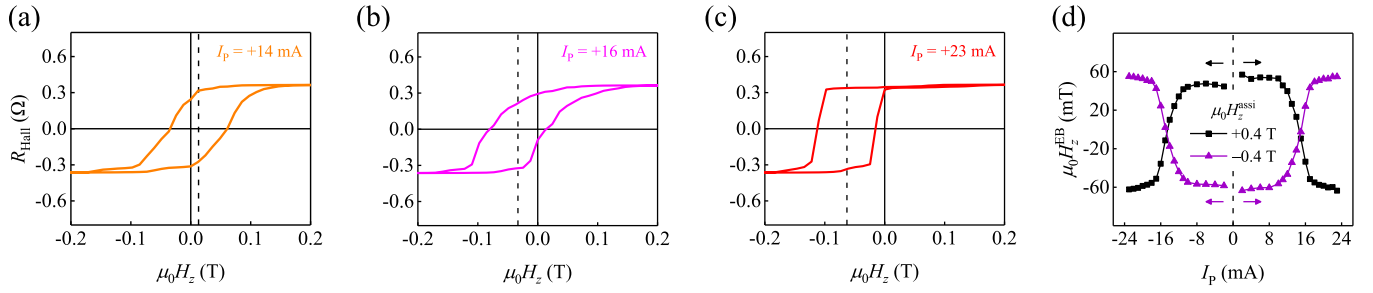


FIG. 3. (a)–(c) Curves showing R_{Hall} versus $\mu_0 H_z$ after writing with an I_p of (a) +14 mA, (b) +16 mA, and (c) +23 mA under a $\mu_0 H_z^{\text{assi}}$ of +0.4 T from the initial state set by applying an I_p of +23 mA under a $\mu_0 H_z^{\text{assi}}$ of -0.4 T. (d) $\mu_0 H_z^{\text{EB}}$ after writing with various I_p under a $\mu_0 H_z^{\text{assi}}$ of +0.4 T (black squares) and -0.4 T (purple triangles). The arrows indicate the current sweep direction.

as the field cooling process, and Joule heating is unavoidable in our experiment. Thermal fluctuation excites AFM spins thermally and imprints FM magnetization into AFM interfacial spins during the cooling process [28]. However, in our experiments, the maximum temperature during application of 1 ms and an I_p of +23 mA is only 363 K at room temperature (see Supplemental Material Fig. S2 [22]). This temperature is far below the reported blocking temperature (450 K to 520 K) of the 8-nm-thick IrMn layer [19,29]. Therefore, the Joule heating effect in our experiment is not sufficient to overcome the energy barrier of interfacial AFM spins solely. However, Joule heating effects should not be neglected because Joule heating is nonzero and always lowers the energy barrier of the interfacial AFM spins. Besides, it is necessary to identify the other contribution of current in the EB manipulations. We consider that the THz excitation of the AFM Néel vector of multigrains via current application is the main origin of the observed EB manipulations. We will explain our deduction as follows.

Recent theoretical predictions have described that an antidamping torque of SOT triggers THz oscillation of the AFM Néel vector in the HM/AFM bilayer [30–33]. Moreover, experimentally observed Néel vector reorientations can be explained by the antidamping SOT-provoked Néel vector oscillation in the HM/AFM structure [8,12,34]. Here, to reveal how the antidamping SOT contributes to current-induced EB manipulation, a macrospin model is introduced in a FM/AFM interface system. Figure 4(a) is a schematic illustration of the current-induced EB switching procedure via AFM oscillation in a FM/AFM interface system. The system consists of FM spin (\mathbf{m}_{FM}), the first AFM sublattice spin (\mathbf{m}_{AFM1}), and the second AFM sublattice spin (\mathbf{m}_{AFM2}) from the bottom, as shown in Fig. 4(a). We modeled a partially uncompensated AFM state by assuming that the exchange coupling energy between \mathbf{m}_{FM} and \mathbf{m}_{AFM1} is larger than that between \mathbf{m}_{FM} and \mathbf{m}_{AFM2} . The finite EB field is embedded as summing the different exchange fields of \mathbf{m}_{FM} from \mathbf{m}_{AFM1} and \mathbf{m}_{AFM2} [35]. This imbalanced exchange-coupling energy in a partially uncompensated AFM state is ascribed to the defects and/or rough interfaces for spin-flop coupling [36,37]. The uniaxial magnetic anisotropy energies of FM and AFM sublattices and the Zeeman energy due to the applied external magnetic field are considered in our model, as well as the exchange energies. To explain polycrystalline IrMn, the uniaxial anisotropy axis of AFM sublattices is defined by the random axis inside the

tilted plane from the z -axis ($\hat{\gamma}$) to the x - y plane [22,38]. Under the aforementioned assumptions, the total magnetic energy (E) is given by the following:

$$\begin{aligned} \frac{E}{M_s} = & -\frac{1}{2} (H_{\text{FM}}^K (\mathbf{m}_{\text{FM}} \cdot \hat{z})^2 + H_{\text{AFM}}^K ((\mathbf{m}_{\text{AFM1}} \cdot \hat{\gamma})^2 \\ & + (\mathbf{m}_{\text{AFM2}} \cdot \hat{\gamma})^2)) \\ & - \sum_{i=1}^3 \left(H_z (\mathbf{m}_i \cdot \hat{z}) + \sum_{j=i+1}^3 H_{ij}^{\text{ex}} (\mathbf{m}_i \cdot \mathbf{m}_j) \right), \quad (1) \end{aligned}$$

where M_s is the saturation magnetization, $H_{\text{FM}/\text{AFM}}^K$ is the uniaxial anisotropy field for the FM and AFM layers, H_z is the external magnetic field, H_{ij}^{ex} is the exchange field, and $\mathbf{m}_{i/j}$ ($i, j = 1, 2, 3$) denotes \mathbf{m}_{FM} , \mathbf{m}_{AFM1} , and \mathbf{m}_{AFM2} , respectively. M_s is assumed to be the same value for FM and AFM sublattices for simplicity.

Subsequently, we numerically solve the coupled Landau-Lifshitz-Gilbert equation including an antidamping SOT based on the FM/AFM interface model discussed in the Supplemental Material S3 [22]. An external magnetic field is constantly applied along the $-z$ direction with the SOT by a current pulse. The physical parameters used in our model simulation are shown Supplemental Material Table SI [22]. Figure 4(b) presents the time evolution of the I_p , and the z components of \mathbf{m}_{AFM2} , \mathbf{m}_{AFM1} , and \mathbf{m}_{FM} as a result of the macrospin calculation. We observe that the z components of \mathbf{m}_{AFM2} and \mathbf{m}_{AFM1} begin to oscillate with a frequency of 0.83 THz during the application of the I_p , which agrees with the aforementioned theoretical predictions [8,30–34]. We note that while the antidamping SOT induces THz oscillation in the AFM layer, m_z^{FM} remains unswitched, which is ascribed to a sufficiently large external magnetic field to overcome the SOT in the FM layer. Figure 4(c) shows the E calculated from Eq. (1) as a function of the angle between the z -axis and the antiferromagnetic sublattice 1 direction in the xz plane (θ_{AFM1}) using the same physical parameters as in Fig. 4(b). There are two local energy minima states in Eq. (1) at $\theta_{\text{AFM1}} = 78^\circ$ and 243° , which are mainly determined by the randomly assigned uniaxial anisotropy axis of the AFM. In this calculation, the anisotropy axis $\hat{\gamma}$ corresponds to the plane tilted 20° away from the z -axis. There is an energy difference between the two energy minima, and the minimum energy state of $\theta_{\text{AFM1}} = 243^\circ$ is lower than the other minimum

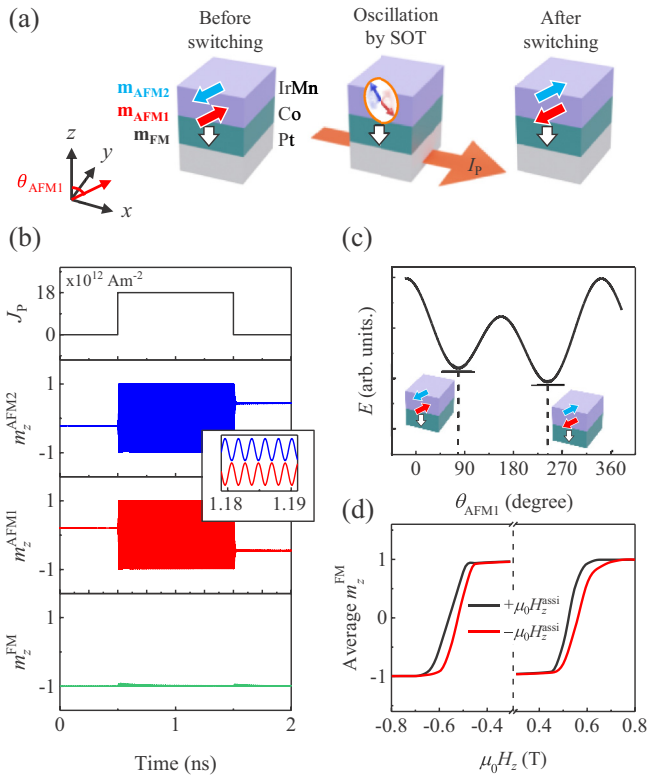


FIG. 4. (a) Schematic illustrations of magnetization configurations of FM \mathbf{m}_{FM} (white arrows), and AFM sublattices \mathbf{m}_{AFM1} (red arrows) and \mathbf{m}_{AFM2} (blue arrows) at each state with current-induced EB switching. (b) Macrospin simulation results. Here, m_z^{FM} (green line), m_z^{AFM1} (red line), and m_z^{AFM2} (blue line) are the z components of \mathbf{m}_{FM} , \mathbf{m}_{AFM1} , and \mathbf{m}_{AFM2} , respectively. J_p is the pulse current density (black line). The inset displays the enlargement of m_z^{AFM1} and m_z^{AFM2} during current pulse application (1.18 ns to 1.19 ns) to show the THz oscillations more clearly. (c) Calculated magnetic energy E as a function of the angle between the z -axis and AFM sublattice 1 in the xz plane, θ_{AFM1} . The insets illustrate the magnetization configurations of the sample at local minima points. (d) Hysteresis loops obtained by sweeping $\mu_0 H_z$ for each simulation and averaging m_z^{FM} over 100 macrospin simulations to mimic the multigrain nature of the polycrystalline sample after switching under a $+\mu_0 H_x^{\text{assist}}$ (black line) and $-\mu_0 H_x^{\text{assist}}$ (red line).

($\theta_{\text{AFM1}} = 78^\circ$). This energy difference is a signature of the EB, the origin of the unidirectional anisotropy nature, and shift of the hysteresis loop of the EB system. The lowest state is determined by coupling with \mathbf{m}_{FM} , which is aligned in the $-z$ direction in this simulation. When turning off the SOT current, the excited AFM spins settle to local ground states. Consequently, \mathbf{m}_{AFM1} has a higher probability of settling along the direction of FM magnetization; therefore, the EB is manipulated along \mathbf{m}_{FM} . The macrospin model presented here provides a comprehensive explanation for both prior findings [16] and our own results, which observed that the manipulated EB field directions are independent of current polarity. When the y -spin polarized spin current causes AFM spins to

oscillate in the xz plane, these spins cease oscillation in a random direction in the xz plane upon turning off the current, and settle along the predefined FM magnetization direction. Consequently, the current polarity becomes irrelevant in the determination of the EB field direction. Additionally, some studies have reported that the EB field directions are determined by the current polarity in the absence of an assist field in HM/AFM/FM structures [19,20]. These observations can also be explained by our macrospin model, which indicates that the SOT induces oscillation of the AFM spins and manipulates the FM state at the same time, ultimately causing the EB field direction to prefer the FM direction; this process is solely influenced by the SOT and hence is dependent on the current polarity.

To provide further evidence to support our model, we implement our model simulation with positive and negative assist magnetic fields ($\pm\mu_0 H_z^{\text{assist}}$). To account for the probabilistic nature of the $\mathbf{m}_{\text{AFM1,2}}$ switching and the collective effect of AFM grains in polycrystalline FM/AFM systems with distributed local crystallographic axes [38,39], simulations are repeated 100 times, and the results are averaged by assuming that each simulation corresponds to a single grain. We introduce a Langevin thermal field with a random direction and amplitude, and distributed anisotropy constants and axes for each simulation. We note that variations in these parameters do not qualitatively change the results. Figure 4(d) presents simulated hysteresis loops obtained by sweeping the z -axis external magnetic field at the final state (time = 2 ns) of each simulation and averaging m_z^{FM} . The hysteric curves of m_z^{FM} are exchange-biased, and the EB field is definitely switched after the application of a pulsed current, depending on the sign of the $\mu_0 H_z^{\text{assist}}$. Nevertheless, the macrospin model is unable to consider the interaction between each domain, the simulation successfully reproduces the experimental EB switching (showing the magnetic configuration of the FM layer), and the SOT-induced AFM oscillation greatly contributes to the current-induced EB manipulation in the HM/FM/AFM heterostructure. Subtle differences in the coercivity and magnitude of the EB field between the calculation and the experimental results are attributed to the single domain approximation of our simulation.

In conclusion, we propose a promising tool for the manipulation of the EB for both out of plane and in plane in HM/FM/AFM heterostructures. Furthermore, our systematic experimental investigations and theoretical analyses, based on a macrospin simulation including a FM/AFM interfacial system, substantiate that current-induced EB manipulation stems from the SOT-induced oscillation of AFM spins and that the magnetic coupling between FM/AFM layers determines the magnitude and direction of the EB field.

This work is supported by the National Research Foundation of Korea (Grants No. 2021R1A2C2007672 and No. 2021M3F3A2A01037525).

[1] T. Jungwirth, X. Marti, P. Wadley, and J. Wunderlich, *Nat. Nanotechnol.* **11**, 231 (2016).

[2] V. Baltz, A. Manchon, M. Tsoi, T. Moriyama, T. Ono, and Y. Tserkovnyak, *Rev. Mod. Phys.* **90**, 015005 (2018).

- [3] T. Jungwirth, J. Sinova, A. Manchon, X. Marti, J. Wunderlich, and C. Felser, *Nat. Phys.* **14**, 200 (2018).
- [4] P. Wadley *et al.*, *Science* **351**, 587 (2016).
- [5] S. Y. Bodnar, L. Šmejkal, I. Turek, T. Jungwirth, O. Gomonay, J. Sinova, A. A. Sapozhnik, H.- J. Elmers, M. Kläui, and M. Jourdan, *Nat. Commun.* **9**, 348 (2018).
- [6] M. J. Grzybowski, P. Wadley, K. W. Edmonds, R. Beardsley, V. Hills, R. P. Champion, B. L. Gallagher, J. S. Chauhan, V. Novak, T. Jungwirth, F. Maccherozzi, and S. S. Dhesi, *Phys. Rev. Lett.* **118**, 057701 (2017).
- [7] P. Wadley, S. Reimers, M. J. Grzybowski, C. Andrews, M. Wang, J. S. Chauhan, B. L. Gallagher, R. P. Champion, K. W. Edmonds, S. S. Dhesi, F. Maccherozzi, V. Novak, J. Wunderlich, and T. Jungwirth, *Nat. Nanotechnol.* **13**, 362 (2018).
- [8] X. Z. Chen, R. Zarzuela, J. Zhang, C. Song, X. F. Zhou, G. Y. Shi, F. Li, H. A. Zhou, W. J. Jiang, F. Pan, and Y. Tserkovnyak, *Phys. Rev. Lett.* **120**, 207204 (2018).
- [9] T. Moriyama, K. Oda, T. Ohkochi, M. Kimata, and T. Ono, *Sci. Rep.* **8**, 14167 (2018).
- [10] L. Baldrati, O. Gomonay, A. Ross, M. Filianina, R. Lebrun, R. Ramos, C. Leveille, F. Fuhrmann, T. R. Forrest, F. Maccherozzi, S. Valencia, F. Kronast, E. Saitoh, J. Sinova, and M. Kläui, *Phys. Rev. Lett.* **123**, 177201 (2019).
- [11] I. Gray, T. Moriyama, N. Sivadas, G. M. Stiehl, J. T. Heron, R. Need, B. J. Kirby, D. H. Low, K. C. Nowack, D. G. Schlom, D. C. Ralph, T. Ono, and G. D. Fuchs, *Phys. Rev. X* **9**, 041016 (2019).
- [12] Y. Takeuchi, Y. Yamane, J.- Y. Yoon, R. Itoh, B. Jinnai, S. Kanai, J. Ieda, S. Fukami, and H. Ohno, *Nat. Mater.* **20**, 1364 (2021).
- [13] H. Tsai, T. Higo, K. Kondou, T. Nomoto, A. Sakai, A. Kobayashi, T. Nakano, K. Yakushiji, R. Arita, S. Miwa, Y. Otani, and S. Nakatsuji, *Nature (London)* **580**, 608 (2020).
- [14] I. K. Schuller, R. Morales, X. Batlle, U. Nowak, and G. Güntherodt, *J. Magn. Magn. Mater.* **416**, 2 (2016).
- [15] J. Wu, D. Carlton, J. S. Park, Y. Meng, E. Arenholz, A. Doran, A. T. Young, A. Scholl, C. Hwang, H. W. Zhao, J. Bokor, and Z. Q. Qiu, *Nat. Phys.* **7**, 303 (2011).
- [16] P.- H. Lin, B.- Y. Yang, M.- H. Tsai, P.- C. Chen, K.- F. Huang, H.- H. Lin, and C.- H. Lai, *Nat. Mater.* **18**, 335 (2019).
- [17] X. H. Liu, K. W. Edmonds, Z. P. Zhou, and K. Y. Wang, *Phys. Rev. Appl.* **13**, 014059 (2020).
- [18] S. Peng, D. Zhu, W. Li, H. Wu, A. J. Grutter, D. A. Gilbert, J. Lu, D. Xiong, W. Cai, P. Shafer, K. L. Wang, and W. Zhao, *Nat. Electron.* **3**, 757 (2020).
- [19] H.- J. Kim, S.- G. Je, D.- H. Jung, K.- S. Lee, and J.- I. Hong, *Appl. Phys. Lett.* **115**, 022401 (2019).
- [20] J. Kang, J. Ryu, J.- G. Choi, T. Lee, J. Park, S. Lee, H. Jang, Y. S. Jung, K.- J. Kim, and B.- G. Park, *Nat. Commun.* **12**, 6420 (2021).
- [21] K. Ando, S. Takahashi, K. Harii, K. Sasage, J. Ieda, S. Maekawa, and E. Saitoh, *Phys. Rev. Lett.* **101**, 036601 (2008).
- [22] See Supplemental Material at <http://link.aps.org/supplemental/10.1103/PhysRevB.107.214403> for magnetic properties of deposited samples, current-induced Joule heating effect, and macrospin simulations. This material includes Ref. [23].
- [23] R. L. Stamps, *J. Phys. D Appl. Phys.* **33**, R247 (2000).
- [24] L. Liu, C.- F. Pai, Y. Li, H. W. Tseng, D. C. Ralph, and R. A. Buhrman, *Science* **336**, 555 (2012).
- [25] I. M. Miron, K. Garello, G. Gaudin, P.- J. Zermatten, M. V. Costache, S. Auffret, S. Bandiera, B. Rodmacq, A. Schuhl, and P. Gambardella, *Nature (London)* **476**, 189 (2011).
- [26] K. Olejník, V. Schuler, X. Marti, V. Novák, Z. Kašpar, P. Wadley, R. P. Champion, K. W. Edmonds, B. L. Gallagher, J. Garces, M. Baumgartner, P. Gambardella, and T. Jungwirth, *Nat. Commun.* **8**, 15434 (2017).
- [27] J. Shi, V. Lopez-Dominguez, F. Garesci, C. Wang, H. Almasi, M. Grayson, G. Finocchio, and P. Khalili Amiri, *Nat. Electron.* **3**, 92 (2020).
- [28] S. Brück, J. Sort, V. Baltz, S. Suriñach, J. S. Muñoz, B. Dieny, M. D. Baró, and J. Nogués, *Adv. Mater.* **17**, 2978 (2005).
- [29] S. K. Mishra, F. Radu, H. A. Dürr, and W. Eberhardt, *Phys. Rev. Lett.* **102**, 177208 (2009).
- [30] R. Cheng, D. Xiao, and A. Brataas, *Phys. Rev. Lett.* **116**, 207603 (2016).
- [31] R. Zarzuela and Y. Tserkovnyak, *Phys. Rev. B* **95**, 180402(R) (2017).
- [32] V. Puliafito, R. Khymyn, M. Carpentieri, B. Azzerboni, V. Tiberkevich, A. Slavina, and G. Finocchio, *Phys. Rev. B* **99**, 024405 (2019).
- [33] H. Fujita, *Phys. Status Solidi RRL* **11**, 1600360 (2017).
- [34] S. Miwa, S. Iihama, T. Nomoto, T. Tomita, T. Higo, M. Ikhlas, S. Sakamoto, Y. Otani, S. Mizukami, R. Arita, and S. Nakatsuji, *Small Science* **1**, 2000062 (2021).
- [35] J. De Clercq, J. Leliaert, and B. Van Waeyenberge, *J. Phys. D Appl. Phys.* **50**, 425002 (2017).
- [36] T. C. Schulthess and W. H. Butler, *Phys. Rev. Lett.* **81**, 4516 (1998).
- [37] T. C. Schulthess and W. H. Butler, *J. Appl. Phys.* **85**, 5510 (1999).
- [38] K. O'Grady, L. E. Fernandez-Outon, and G. Vallejo-Fernandez, *J. Mag. Magn. Mater.* **322**, 883 (2010).
- [39] A. van den Brink, G. Vermijs, A. Solignac, J. Koo, J. T. Kohlhepp, H. J. M. Swagten, and B. Koopmans, *Nat. Commun.* **7**, 10854 (2016).